Reconstructing Ocean Surface Current Combining Altimetry and Future Spaceborne Doppler Data

Clement Ubelmann, Gérald Dibarboure, Lucile Gaultier, Aurélien Ponte and Fabrice Ardhuin

May 27, 2020

Contents

1 Summary

Two methods for the mapping of ocean surface currents from satellite measurements of sea level and future current vectors are presented and contrasted. Both methods rely on the linear and Gaussian analysis framework, but with different levels of covariance definitions. The first method separately maps sea level and currents with single-scale covariance functions and leads to estimates of the geostrophic and ageostrophic circulations. The second maps both measurements simultaneously and projects the circulation onto 4 contributions: geostrophic, ageostrophic rotary, ageostrophic divergent and inertial. When compared to the first method, the second mapping moderately improves the resolution of geostrophic currents but significantly improves estimates of the ageostrophic circulation, in particular near-inertial oscillations. This method offers promising perspectives for reconstructions of the Ocean surface circulation for both slow (>5days) and fast (hourly) scales from future Doppler instruments even with moderate time revisits constrained by the orbits and instrument designs.

2 Introduction

The Ocean surface current, a key variable for many scientific and operational applications, is only partially and indirectly observed from space. Altimetry provides the geostrophic component (Fu et al., 1988), important at the mesoscale in most of the Oceans, but limited to about 150-200km effective resolution in wavelength (Ballarotta et al., 2019). The ageostrophic component, not synoptically observed yet, is only locally sampled from drifting buoys (Elipot et al., 2016) or High Frequency Radars near the costs (Kim et al., 2008). If model estimates for ageostrophic current are available, in particular for the low-frequency part (Rio et al., 2014) the uncertainties are still high. Filling this gap with satellite measurements of the total surface current is the topic of active research, with several emerging concepts of spaceborne Doppler radar such as SKIM (F. Ardhuin et al., 2019b) or WaCM (Rodriguez et al., 2018). Similarly to HF radar, these later would provide radial components for multiple look angles, from which the two-dimentional current vector could be assessed.

As for any satellite observation of a geophysical variable evolving in time and space, an important question is the ability to map the field given the instrument spatial resolution and time revisits. The case of altimetry was interesting, since the Sea Surface Height (SSH) contains the signature of various processes in the Ocean spanning over a wide range of scales, some at a much higher frequency than the typical 10-day revisits of the Jason satellite orbits for instance. But these later (in particular barotropic tides and response to high frequency winds and pressure) turned out to be well handled either from independent or empirical models, allowing accurate reconstructions of the mesoscale eddy field and derived geosprophic currents (Le Traon and Dibarboure, 2002) with limited aliasing contamination. The case of total surface current now brings new challenges. Indeed, the response to high frequency winds is a strong component, both in open and coastal Oceans, leading to Near Inertial Oscillations (NIO) (D'Asaro, 1985) which have typical rms of 10-15 cm/s at mid and high latitudes (Elipot et al., 2010), often comparable to mesoscale magnitudes. If the physical processes are well understood and modelled (Pollard and Millard, 1970, D'Asaro, 1985, Kim et al., 2014), the predictability, especially in phase, is not yet accurate (for instance, a few hours offset in the wind reanalysis would disturb the phase leading to wrong predictions). Relying on independent models of the high-frequency surface current is therefore not yet guaranteed. Although Doppler radar concepts may allow shorter time revisits than altimetry thanks to relatively wide swaths (Rodriguez et al., 2018), it would not correctly sample inertial periods (e.g. 18 hours at 40° N/S). Therefore, the reconstruction of surface current in time and space from space-borne doppler is a challenge, beyond the technological aspects.

The focus of this paper is to explore this reconstruction challenge in simulation, from the SKIM concept combined with altimetry, using basic and improved mapping methods accounting for NIO physical properties. The skills of reconstruction will be evaluated quantitatively for both geostrophic and ageostrophic components in the North Atlantic basin.

3 Reconstruction methods

3.1 Background on linear analysis

The different mapping approaches explored in this study are all derived from the linear and Gaussian mapping framework reminded in this paragraph.
We assume a vector of observations, noted $\mathbf{y}$ that can be related to the state to estimate, noted $\mathbf{x}$, with a linear operator $\mathbf{H}$ such as:

$$\mathbf{y} = \mathbf{H}\mathbf{x} + \epsilon \tag{1}$$

where ϵ is an independent observation error. If we define $\mathbf{B}$ the covariance matrix of $\mathbf{x}$ and $\mathbf{R}$ the covariance matrix of the error vector ϵ, both variables being assumed Gaussian, then the linear estimate writes:

$$\mathbf{x^a} = \mathbf{B}\mathbf{H^T}(\mathbf{H}\mathbf{B}\mathbf{H^T} + \mathbf{R})^{-1}\mathbf{y} \tag{2}$$

This formulation, known as Optimal Interpolation, requires a matrix inversion in observation space (size of $\mathbf{y}$). When the number of observations exceeds the size of the state to resolve, it can be interesting to use an equivalent formulation given by the Sherman-Morrison-Woodbury transformation, allowing inversion in state space (size of $\mathbf{x}$):

$$\mathbf{x^a} = (\mathbf{H^T}\mathbf{R^{-1}}\mathbf{H} + \mathbf{B^{-1}})^{-1}\mathbf{H^T}\mathbf{R^{-1}}\mathbf{y} \tag{3}$$

This formulation is particularly useful when considering transformed states expressed in orthogonal bases (see section 3.3.1) as $\mathbf{B}$ becomes diagonal and the whole system gets easier to invert.
If we note $\mathbf{K}$ the linear operator such as $\mathbf{x^a} = \mathbf{K}\mathbf{y}$, either expressed from Eq.2 or Eq.3, the covariance matrix of analysis error writes:

$$\mathbf{B^a} = (\mathbf{I} - \mathbf{K}\mathbf{H})\mathbf{B} \tag{4}$$

This later can be used to characterize the uncertainty of the solution.

3.2 Basic mappings

In the basic mapping approaches, we perform separate mappings of the SSH and total surface current involving simple covariance functions in the $\mathbf{B}$ matrix defined separately for each variable. Then the geostrophic component is given by the derivation of SSH maps and the ageostrophic component by subtraction of the geostrophic component from the mapped total current.

3.2.1 For SSH: the standard Aviso/CMEMS mapping

To map the SSH, we first map the Sea Level Anomaly (SLA), defined in reference to the long-term mean. We followed, as in the standard Aviso/CMEMS mapping, a basic formulation derived from Eq.2. The observation vector $\mathbf{y}$ is the SLA observations, noted $\mathbf{h^o}$. The state vector $\mathbf{x}$ is the gridded SLA. The observation operator $\mathbf{H}$ is a simple tri-linear interpolator tranforming the gridded state SLA to equivalent along-track SLA.
Since the covariance of SLA (represented by the $\mathbf{B}$ matrix) is assumed to vanish beyond a few hundreds of kilometers in space and beyond 10 to 20 days in time ((Le Traon and Dibarboure, 2002)), separate inversions are performed locally selecting observations over time and space windows adjusted to these values. In practice, the number of observations being limited to less than 1000, the inversion in observation space is computationally manageable. Details on the covariance model and map production are given in (Pujol et al., 2016). From the SLA maps, the SSH maps are given with the addition of the long-term mean subtracted before the mapping.

3.2.2 For total surface current: a bi-variate weighted least square

To map the total surface current, we followed a basic formulation derived from Eq.3. The observation vector $\mathbf{y}$ is the radial velocities noted $\mathbf{u_r^o}$. The state vector $\mathbf{x}$ is the concatenation of the gridded current in the zonal and meridional directions noted $[\mathbf{u}, \mathbf{v}]^\mathbf{T}$.
If θ is the vector of look angle for the radial current vector $\mathbf{u_r^o}$, the linear observation operator $\mathbf{H}$ is a tri-linear-interpolator-projector whom the projection component $\mathbf{H_v}$ writes:

$$\mathbf{H_v} = \begin{bmatrix} cos(\theta_1) & sin(\theta_1) \\ \vdots & \vdots \\ cos(\theta_p) & sin(\theta_p) \end{bmatrix} \tag{5}$$

where p is the number of observations.
Considering no a priori on the signal covariances ($\mathbf{B^{-1}} = \mathbf{0}$), Eq.3 becomes the following least square formula:

$$[\mathbf{u}, \mathbf{v}]^\mathbf{T} = (\mathbf{H^T R^{-1} H})^{-1} \mathbf{H^T R^{-1} u_r^o} \tag{6}$$

with the covariances of analysis given by the limit of Eq.4 when $\mathbf{B}$ tends to infinity:

$$\mathbf{B^a} = \mathbf{H^T R^{-1} H} \tag{7}$$

Since $\mathbf{B}$ is considered infinite, a selection window in time and space is defined to implicitly apply temporal and spatial filtering parameters of the estimated signal. This later must be large enough to ensure invertibility of Eq.6, i.e. including at least two observations at different θ angles. The $\mathbf{R}$ matrix represents the covariances of $\mathbf{u_r^o}$ errors, assumed diagonal (independent errors between Doppler measurements). Note that $\mathbf{R^{-1}}$ can also be called the weight matrix $\mathbf{W}$, the weights being the inverse of observation error variances. A geometrical illustration of the solution is shown in Figure 1, with the ellipses of the solution uncertainty given by the $\mathbf{B^a}$ matrix of size (2×2).

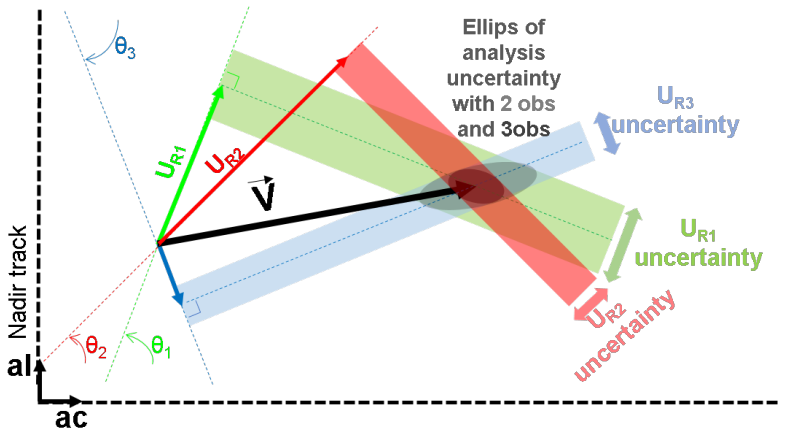

Figure 1: Scheme of the basic surface current mapping algorithm based on a bi-variate weighted least square, from at least two radial doppler observations at different look angles

In practice, for the problem considered in section 4, the spatial and temporal windows will be set to 40km diameter and 10 days respectively. The observation error variances in $\mathbf{W}$ will be set to 0.2^2 $(m/s)^2$ which includes the intrumental error and the representativity error imposed by the time and space window filtering.

3.2.3 Geostrophic and ageostrophic current gridded maps

The geostrophic current $(\mathbf{u_g}, \mathbf{v_g})$ is directly derived from the mapped SSH:

$$\begin{cases} u_g = -\frac{g}{f_c}\frac{\partial SSH}{\partial y} \\ v_g = \frac{g}{f_c}\frac{\partial SSH}{\partial x} \end{cases} \tag{8}$$

where f_c is the Coriolis frequency function of latitude. Then, the ageostrophic estimates $(\mathbf{u_{ag}}, \mathbf{v_{ag}})$ are obtained by substraction to the total surface current $(\mathbf{u}, \mathbf{v})$ of 3.2.2:

$$\begin{cases} u_{ag} = u - u_g \\ v_{ag} = v - v_g \end{cases} \tag{9}$$

These geostrophic and ageostrophic current estimates will be considered as the basic mapping solutions in section 5

3.3 Improved mapping

The improved mapping also relies on linear analysis framework but with extended state, extended observation vector and multivariate covariances. For practical reasons, the inversion problem is framed in a reduced component space such as to accomodate the large number of observations in spatiotemporal windows. This is particularly interesting to handle multiple signals of various scales in time and/or space.

3.3.1 Formulation

We consider an extended state vector defined by the concatenation of surface topography and surface current:

$$\mathbf{x} = (\mathbf{h}, \mathbf{u}, \mathbf{v})^{\mathbf{T}} \tag{10}$$

and an observation vector also extended to topography and radial current:

$$\mathbf{y} = (\mathbf{h^o}, \mathbf{u_r^o})^{\mathbf{T}} \tag{11}$$

Consequently, the operator $\mathbf{H}$ is the combination of the tri-linear interpolator $\mathbf{H_h}$ defined in section 3.2.1 (transforming h into equivalent along-track SLA) and the tri-linear interpolator-projector $\mathbf{H_v}$ defined in section 3.2.2 (transforming (u, v) into colocated radial current at observation location):

$$\mathbf{H} = \begin{bmatrix} H_h & H_v \end{bmatrix} \tag{12}$$

Also, the state $\mathbf{x}$ can be considered as the sum of N components (e.g. geostrophy, low and high frequency ageostrophy as proposed in section 3.3.3) noted:

$$\mathbf{x} = \sum_{\mathbf{k=1}}^{\mathbf{N}} \mathbf{x_k} \tag{13}$$

considered in the following as independent (zero covariances between components).
We also assume that each individual component $\mathbf{x_k}$ can be expressed as the sum of independent multi-variate sub-components written in a matrix $\mathbf{\Gamma_k}$ (that can be spatio-temporal EOFs or wavelet bases as detailed in 3.3.2):

$$\mathbf{x_k} = \begin{bmatrix} \Gamma_{k,h} \\ \Gamma_{k,u} \\ \Gamma_{k,v} \end{bmatrix} \eta_{\mathbf{k}} = \mathbf{\Gamma_k}\eta_{\mathbf{k}} \tag{14}$$

where $\eta_{\mathbf{k}}$ is the vector of coefficients for each sub-component written in the columns of Γ_k.

If we note:

$$\mathbf{\Gamma} = \begin{bmatrix} \Gamma_{1,h} & \dots & \Gamma_{N,h} \\ \Gamma_{1,u} & \dots & \Gamma_{N,u} \\ \Gamma_{1,v} & \dots & \Gamma_{N,v} \end{bmatrix} \tag{15}$$

and

$$\eta = \begin{bmatrix} \eta_1 \\ \vdots \\ \eta_N \end{bmatrix} \tag{16}$$

Eq.13 gives:

$$\mathbf{x} = \mathbf{\Gamma}\eta \tag{17}$$

and using Eq.1, $\mathbf{y} = \mathbf{H\Gamma}\eta + \epsilon$. If we note $\mathbf{G} = \mathbf{H\Gamma}$:

$$\mathbf{y} = \mathbf{G}\eta + \epsilon \tag{18}$$

$\mathbf{G}$ is the expression of the ensemble of sub-components in the observation space. It is noted:

$$\mathbf{G} = \begin{bmatrix} G_{1,h} & \dots & G_{N,h} \\ G_{1,u_r} & \dots & G_{N,u_r} \end{bmatrix} \tag{19}$$

where the columns of $\mathbf{G_{k,h}}$ and $\mathbf{G_{k,u_r}}$ are the sub-components of component k in the observation space.
If we note $\mathbf{Q}$ the covariance matrix for the state vector η , the analyzed solution is:

$$\eta^{\mathbf{a}} = (\mathbf{G^T R^{-1} G} + \mathbf{Q^{-1}})^{-1} \mathbf{G^T R^{-1} y} \tag{20}$$

Since each component and sub-components are assumed independent, $\mathbf{Q}$ is diagonal and expressed as the concatenation of the diagonal matrices $\mathbf{Q_n}$ for each component:

$$\mathbf{Q} = \begin{bmatrix} Q_1 & & \\ & \ddots & \\ & & Q_N \end{bmatrix} \tag{21}$$

Finally, from $\eta^{\mathbf{a}}$, the state in physical space $\mathbf{x^a}$ is obtained applying Eq.17 to $\eta^{\mathbf{a}}$
This formulation (summarized by Eq.17 and Eq.20) is directly derived from the formulation in 3.3.1, with equivalent state covariance $\mathbf{B}$ writing:

$$\mathbf{B} = \mathbf{\Gamma Q \Gamma^T} \tag{22}$$

The choice of the sub-component bases $\mathbf{\Gamma}$ with associated variances $\mathbf{Q}$ is essential as it defines the covariance models in physical space for each component, as discussed in the next section.

3.3.2 Application to simultaneous mapping of geostrophy, low and high frequency ageostrophy

We propose to apply the above formulation for four components ($N = 4$), considering that the surface current is dominated by geostrophy, low frequency ageostrophy (slitting in rotationnal and divergent flows) and high frequency ageostrophy, for which specific wavelet bases will be defined.

3.3.2.1 Geostrophy

Geostrophy is the component that has a signature on both $\mathbf{h}$ and $\mathbf{u_r}$, where to expect some synergy between the Altimetry and Doppler observations. Out of the Tropical band, the current field (U_1, V_1) writes:

$$\begin{cases} U_1 = -\frac{g}{f_c}\frac{SSH}{dy} \\ V_1 = \frac{g}{f_c}\frac{SSH}{dx} \end{cases} \tag{23}$$

To approximate standard covariance models used in Altimetry mapping with the sub-components $\mathbf{\Gamma_1}$ for geostrophy, we propose a local Fourier-based decomposition, with time and space local elements defined by the following formulation:

$$\begin{cases} \Gamma_{1,h}[i,p] = cos(k_{x,p}(x_i - x_p) + k_{y,p}(y_i - y_p) + \Phi_p) * f_{tap}(\frac{x_i - x_p}{L_{x_p}}, \frac{y_i - y_p}{L_{y_p}}, \frac{t_i - t_p}{L_{t_p}}) \\ \Gamma_{1,u}[i,p] = -\frac{g}{f_c}\frac{\partial \Gamma_{1,h}[i,p]}{\partial x_i} \\ \Gamma_{1,v}[i,p] = \frac{g}{f_c}\frac{\partial \Gamma_{1,h}[i,p]}{\partial y_i} \end{cases} \tag{24}$$

where i and p are the line and column indices in observation and state space respectively. Φ_p is alternatively 0 and $\pi/2$, such as all subcomponents are defined by pairs of cardinal sine and cosine functions to allow the phase degree of freedom. $k_{x,p}$ and $k_{y,p}$ are zonal and meridional wavenumbers respectively, set to vary in the mapable mesoscale range, typically 80km to 800km. The function f_{tap} localizes the sub-component in time and space (at scales L_{t_p}, L_{x_p} and L_{y_p} respectively) as geostrophy has local extension of covariances. It is expressed as:

$$f_{tap}(\delta x, \delta y, \delta t) = \begin{cases} cos(\pi \delta x/2) * cos(\pi \delta y/2) * cos(\pi \delta t/2), & \text{for} \quad (|\delta x|, |\delta y|, |\delta t|) < (1,1,1) \\ 0, & \text{elsewhere} \end{cases} \tag{25}$$

In practice, for the problem considered in section 4, L_{x_p} and L_{y_p} will be set to 1.5 the wavelength of element p and L_{t_p} to the decorrelation time scale of Aviso maps, on the order of 10 days in this region.
As an illustration, $\Gamma_{1,h}[:,p]$ is shown on Figure2 upper left panel, in plain color and $\Gamma_{1,u}[:,p]$, $\Gamma_{1,v}[:,p]$ in arrows. Here, this p^{th} component has a dominant wavelength $\lambda = \frac{2\pi}{\sqrt{k_{x,p}^2 + k_{y,p}^2}}$ in a given direction. The lower-left panel represents the temporal extension of the sub-component set by L_{t_p}. The whole time-space domain is therefore paved with similar sub-components, for wavelengths between 80km and 800km spanning in all directions of the plane. The ensemble can be seen as a wavelet basis. Finally, each sub-component is affected an expected variance in the $\mathbf{Q_1}$ matrix, consistent with the power spectrum observed from altimetry at the corresponding wavelength with isotropy assumption.
For a given point i on the time-space grid (312°E,40°N, day 10), the representor $\mathbf{\Gamma_{1,h}[i,:]Q\Gamma_{1,h}}$ is plotted on Figure3 , shown as a function of space (left panel) and as a function of time (right panel). It illustrates the equivalent covariance function, which is quite similar to what is currently used for altimetry mapping with OI inverted in observation space.
As mentioned in section 3.3.1, the inversion involves the construction of $\mathbf{G_1}$ matrix (see Eq.20 and Eq.19), whose p^{th} column is represented on the right panel of Figure2 considering altimetry tracks and scattered radial velocity observations at various look angles described later in section 4. Here, the arrows are the projection of the $(\Gamma_{1_u}[:,p], \Gamma_{1_u}[:,p])$ along the various instrument look angles and the colored dots the bilinear interpolation at nadir altimetry coordinates.

3.3.2.2 Low-frequency ageostrophy: rotational part

For simplicity in the definition of the covariance models, we assume two distinct ensembles of sub-components: the first for a rotational field and the second for a divergent field (following an Helmholtz decomposition). Even though physical interaction surely exist between rotational and divergent ageostrophic flows, we assume them as statistically independent. This paragraph deals with the rotational flow, defined by a potential $\mathbf{P}$ such as the surface current (U_2, V_2) writes:

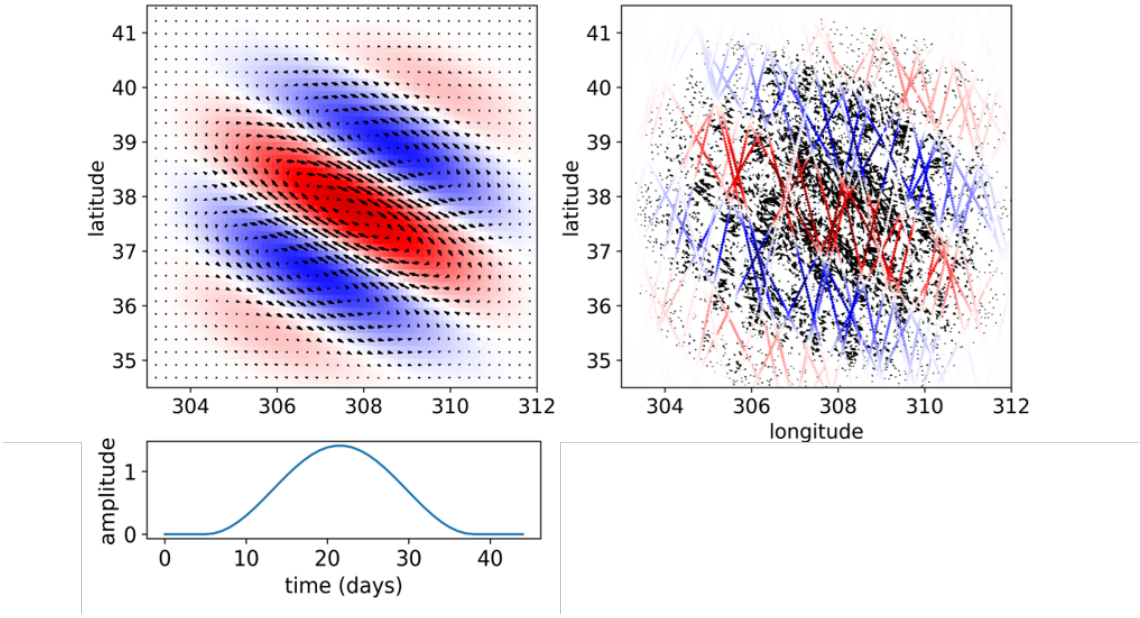

Figure 2: Illustration of a sub-component belonging to the mesoscale geostrophic component. The upper-left panel represents its expression in the grid space (= a column of the $\mathbf{\Gamma_1}$ matrix), in color for the topography ($\mathbf{\Gamma_{1_h}}$) and arrows for the current ($\mathbf{\Gamma_{1_u}}$ and $\mathbf{\Gamma_{1_v}}$), as a function of space. The lower-left panel represent the temporal modulation. The right panel represents the same sub-component in observation space considering altimetry tracks and scattered radial velocity observations at various look angles, noted $\mathbf{G_1}$ declined in $\mathbf{G_{1_h}}$ (colors) and $\mathbf{G_{1_{u_r}}}$ (arrows).

$$\begin{cases} U_2 = -\frac{\partial P}{\partial y} \\ V_2 = \frac{\partial P}{\partial x} \end{cases} \tag{26}$$

Then the $\mathbf{\Gamma_2}$ matrix writes:

$$\begin{cases} \Gamma_{2,h}[i,p] = 0 \\ \Gamma_{2,u}[i,p] = -\frac{\partial \Gamma_{2,P}[i,p]}{\partial x_i} \\ \Gamma_{2,v}[i,p] = \frac{\partial \Gamma_{2,P}[i,p]}{\partial y_i} \end{cases} \tag{27}$$

where $\mathbf{\Gamma_{2,P}}$ is an ensemble of sub-components for P defined in space and time by the function $f_{tap}(\frac{x_i - x_p}{L_{x_p}}, \frac{y_i - y_p}{L_{y_p}}, \frac{t_i - t_p}{L_{t_p}})$ (defined by Eq. 25). In practice, for the problem considered in section 4, L_x and L_y will be both set to 500km and L_t to 5 days.
$\mathbf{\Gamma_{2,h}} = \mathbf{0}$ since we assume no signature of ageostrophy on SSH. The p^{th} column of $(\mathbf{\Gamma_{2,u}}, \mathbf{\Gamma_{2,v}})$ is represented on Figure4.
Here again, the whole time-space domain is paved with similar wavelet sub-components. As opposed to the geostrophy model, we did not chose spectrally-narrow elements as we do not aim to assume specific variance as a function of wavelength (we do not have precise spectral content as we could have for geostrophy from altimetry). The spatial extension of the sub-components, given by L_x, drives the equivalent spatial decorrelation scale of the rotational flow. The temporal extension is defined similarly to the geostrophic model, also with L_t.
The equivalent covariance model obtained from Eq.22, not shown, is overall similar to what is shown on Fig.2 for geostrophy, with a more basic spatial function driven by (L_x, L_y) only. It is set larger in space and shorter in time , aiming to capture large and more rapid signals than geostrophy. Targeting shorter scales in space would not be compatible with the observation dataset considered. In practice, for the problem considered in section 4, they were set to 400km and 5 days in space and time, ensuring enough observations to resolve the total current at this space/time scale.

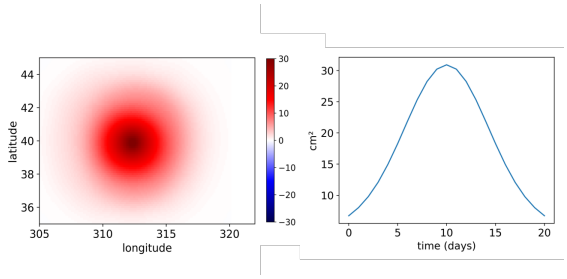

Figure 3: Illustration of the representor $\mathbf{\Gamma_{1_h}}[\mathbf{i},:]\mathbf{Q}\mathbf{\Gamma_{1_h}}$ for a given point i on the time-space grid (312°E,40°N, 10 days)represented as a function of space at 10 days (left panel) and as a function of time at 312°E,40°N.

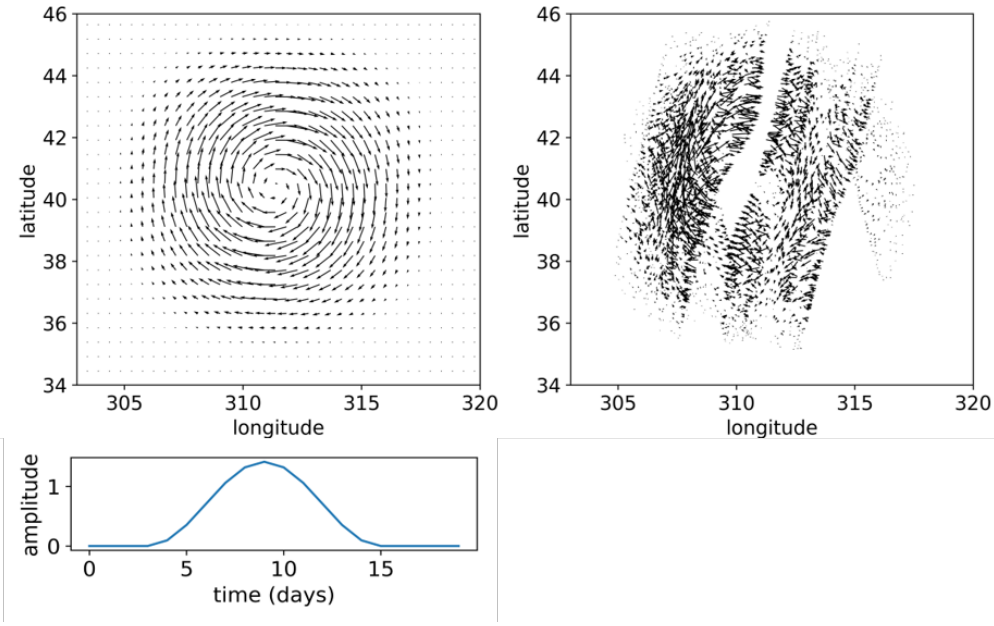

Figure 4: Illustration of a sub-component belonging to the low-frequency ageostrophic rotational component. The upper-left panel represents its expression in the grid space (= a column of the $\mathbf{\Gamma_2}$ matrix), the arrows for ($\mathbf{\Gamma_{2_u}}$ and $\mathbf{\Gamma_{2_v}}$), as a function of space. The lower-left panel represent the temporal modulation. The right panel represents the same sub-component in observation space , noted $\mathbf{G_{2_{ur}}}$.

The p^{th} column of $\mathbf{G_2}$ matrix involved in the inversion is shown on the right panel of Figure 4 for illustration. It represents the projection of the sub-component vector field at the location and look-angle of all observations in the local domain.

3.3.2.3 Low-frequency ageostrophy: divergent part

The divergent part is handled exactly the same way as the rotational part, except that the surface current(U_3, V_3) is defined by a solenoidal function $\mathbf{S}$ such as:

$$\begin{cases} U_3 = -\frac{\partial S}{\partial x} \\ V_3 = -\frac{\partial S}{\partial y} \end{cases} \tag{28}$$

where $\mathbf{U_3}$ and $\mathbf{V_3}$ are the zonal and meridian components of the divergent field. Then the $\mathbf{\Gamma_3}$ matrix writes:

$$\begin{cases} \Gamma_{3,h}[i,p] = 0 \\ \Gamma_{3,u}[i,p] = -\frac{\partial \Gamma_{3,S}[i,p]}{\partial x_i} \\ \Gamma_{3,u}[i,p] = -\frac{\partial \Gamma_{3,S}[i,p]}{\partial y_i} \end{cases} \tag{29}$$

where $\mathbf{\Gamma_{3,S}}$ is an ensemble of sub-components for S that will be defined exactly as for the rotational flow described in paragraph 3.3.2.2, with the same (L_x, L_y) in the implementation section 4.
The p^{th} column of $(\mathbf{\Gamma_{3,u}}, \mathbf{\Gamma_{3,v}})$ is represented on the left panel of Figure5 for illustration, as well as the $\mathbf{G_2}$ matrix involved in the inversion.

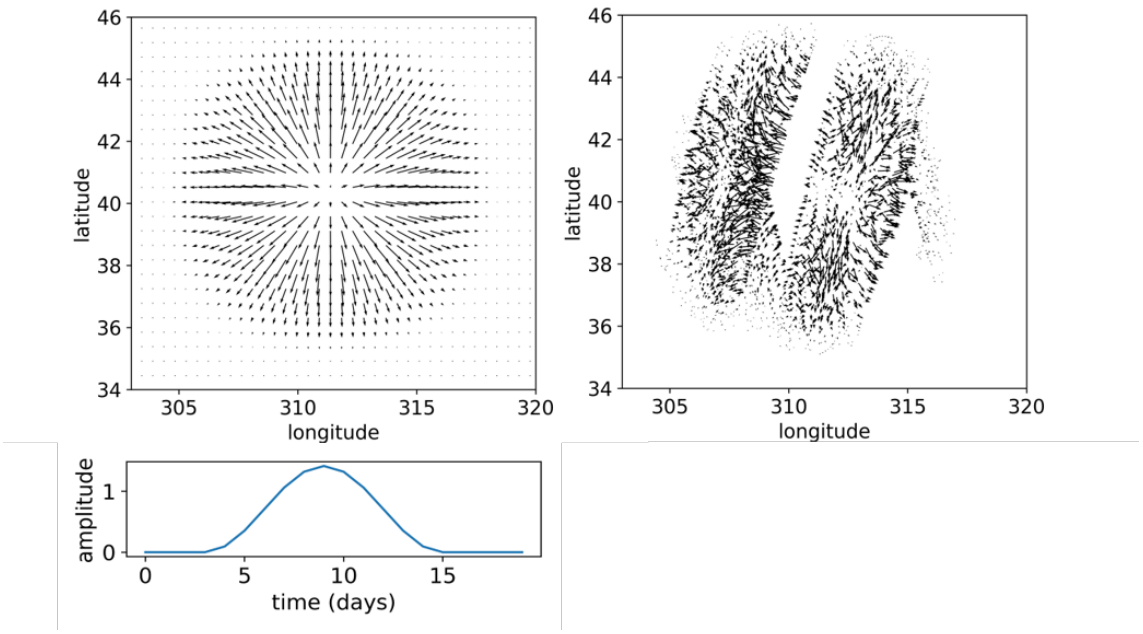

Figure 5: Illustration of a sub-component belonging to the low-frequency ageostrophic divergent component. The upper-left panel represents its expression in the grid space (= a column of the $\mathbf{\Gamma_3}$ matrix), the arrows for ($\mathbf{\Gamma_{3_u}}$ and $\mathbf{\Gamma_{3_v}}$), as a function of space. The lower-left panel represent the temporal modulation. The right panel represents the same sub-component in observation space, noted $\mathbf{G_{3_{u_r}}}$.

3.3.2.4 High-frequency ageostrophy

The near inertial motions are also considered as a distinct component statistically independent. The surface current field (U_4, V_4) can be expressed as follows:

$$\begin{cases} U_4 = Acos(-2\pi f_c t + \phi) \\ V_4 = Asin(-2\pi f_c t + \phi) \end{cases} \tag{30}$$

where f_c is the Coriolis frequency, A and ϕ are slowly (w.r.t. $\frac{1}{f_c}$) evolving functions of space and time . In these conditions, the Γ_4 matrix can be written with the following modes featuring a dominant oscillation at inertial frequency:

$$\begin{cases} \Gamma_{4,h}[i,p] = 0 \\ \Gamma_{4,u}[i,p] = cos(-2\pi f_c(t_i - t_p) + \Phi_p) * e^{-\frac{|t_i - t_p|^q}{\tau^q}} f_{tap}(\frac{x_i - x_p}{L_x}, \frac{y_i - y_p}{L_y}, 0) \\ \Gamma_{4,v}[i,p] = sin(-2\pi f_c(t_i - t_p) + \Phi_p) * e^{-\frac{|t_i - t_p|^q}{\tau^q}} f_{tap}(\frac{x_i - x_p}{L_x}, \frac{y_i - y_p}{L_y}, 0) \end{cases} \tag{31}$$

τ represents a typical decoherence time for the q exponential decay law, L_x and L_y are the spatial decorrelation scales. For the problem considered in section 4, L_x and L_y will be both set to 250km, q at 2 and τ at 3 days. These values were optimized to fit the covariance properties of the NIO signal in the reference simulation.
Here again, $\mathbf{\Gamma_{4_h}} = \mathbf{0}$ as we assume that NIO have no SSH signatures. The p^{th} column of $(\Gamma_{4_u}, \Gamma_{4_v})$ is represented on the left panels of Figure6 for illustration. The arrows on the upper panel indicate a spatially coherent pattern of NIOs, actually rotating in time as indicated by the time-modulation on the lower panel.

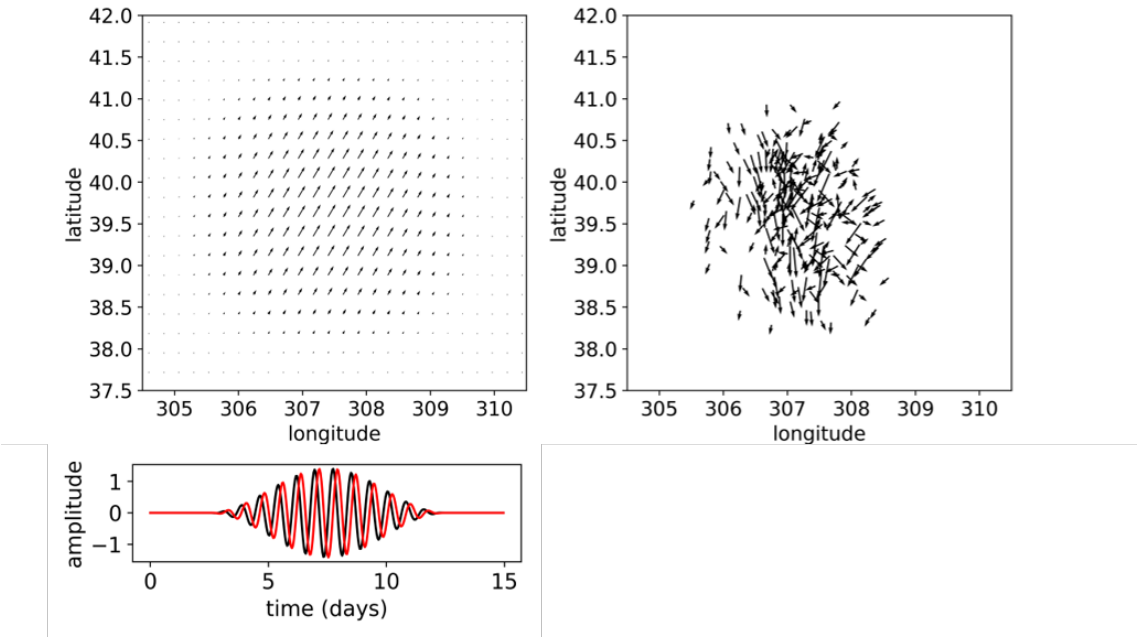

Figure 6: Illustration of a sub-component belonging to the high-frequency ageostrophic component. The upper-left panel represents its expression in the grid space (= a column of the $\mathbf{\Gamma_4}$ matrix), the arrows for ($\mathbf{\Gamma_{4_u}}$ and $\mathbf{\Gamma_{4_v}}$), as a function of space. The lower-left panel represent the temporal modulation for the zonal (black) and meridional (red) components. The right panel represents the same sub-component in observation space, noted $\mathbf{G_{4_{u_r}}}$.

Finally, the p^{th} column of $\mathbf{G_2}$ matrix involved in the inversion is shown on the right panel of Figure 6. The arrows indicate multiple directions are the observations span over different times in the local domain of the sub-component.

3.3.3 Global inversion

From the $\mathbf{G_k}$ matrices mentioned above, each representing a different physical component, we build the concatenated $\mathbf{G}$ matrix followin Eq.19. Resolving Eq.20 will find the coefficients η such as the sum of all sub-components of all components (as represented on the right panels of Figures 2, 4, 5, 6), $\mathbf{G}\eta$, gets close to the actual observation values $\mathbf{y} = (\mathbf{h^o}, \mathbf{u_r^o})^\mathbf{T}$ with respect to the prescribed variances $\mathbf{Q}$ for η.

Once $\eta^\mathbf{a}$ is computed, the solution of each mode n is written on the grid using Eq. 17.

4 Observing System Simulation Experiments

4.1 The reference scene

Ocean circulation numerical models provide realistic scenes of Ocean variability, useful to assess the impact of existing and future observing systems.
In this study, we used the outputs of a high-resolution (1/60° in the horizontal) simulation at hourly frequency, the NEMO NATL60-CJM simulation further described in (Amores et al., 2018).

This simulation, forced with hourly winds, allows the resolution of a wide spectrum of processes at Ocean surface, from basin to sub-mesoscales and from annual to hourly scales including NIOs, in the North Atlantic region. The SSH and surface current in the first layer constitute our ground-truths in the experiments spanning over the year 2012.

4.2 Synthetic observations from instrument simulators

The instrument simulators are based on existing softwares used to generate synthetic observations. They perform a sampling, in time and space, of the reference scene over the satellite view along the orbit, and generate a realistic measurement error, either instrumental or geophysical.

4.2.1 The altimetry simulator

The altimetry simulator (Gaultier et al., 2016) in its nadir version was used in this study to simulate a constellation of 5 altimeters on different orbits (two Jason-like and three Sentinel3-like). The model SSH was sampled at 1 Hz posting (approximately 6 km) along these orbit tracks over 1-year. An instrumental error of 3cm RMS at 1Hz was applied to all satellites following a random Gaussian law to simulate the white-noise plateau. An illustration of the altimetry dataset is shown on the top panels of Figure 7.

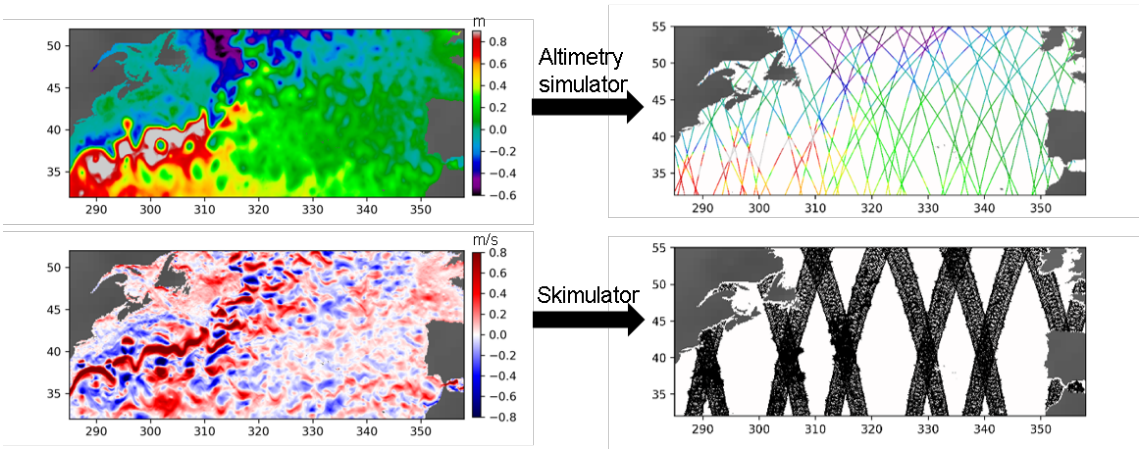

Figure 7: Schematic showing the instrument simulator sampling (altimetry on the top, doppler current Skimulator on the bottom) from the reference scene on the left to the sampled data with instrument error added on the right. Three-day worth of synthetic data are shown on the right panels.

4.2.2 The Doppler simulator

The Doppler simulator for the Skim concept, called 'Skimulator' (Gaultier, 2019b, Gaultier, 2019a), was developed in the context of the Skim Phase A studies. The tool was applied on the first-layer vector current of the reference field, providing radial current vectors along multiple look-angles of the rotating beams as illustrated by the green arrows on Figure 8. An instrument error is applied, accounting for radar noise and Doppler processing errors such as the error in the surface wave Doppler retrieval, as further described in (F. Ardhuin et al., 2019a).The total error is on the order of 5-10 cm/s.

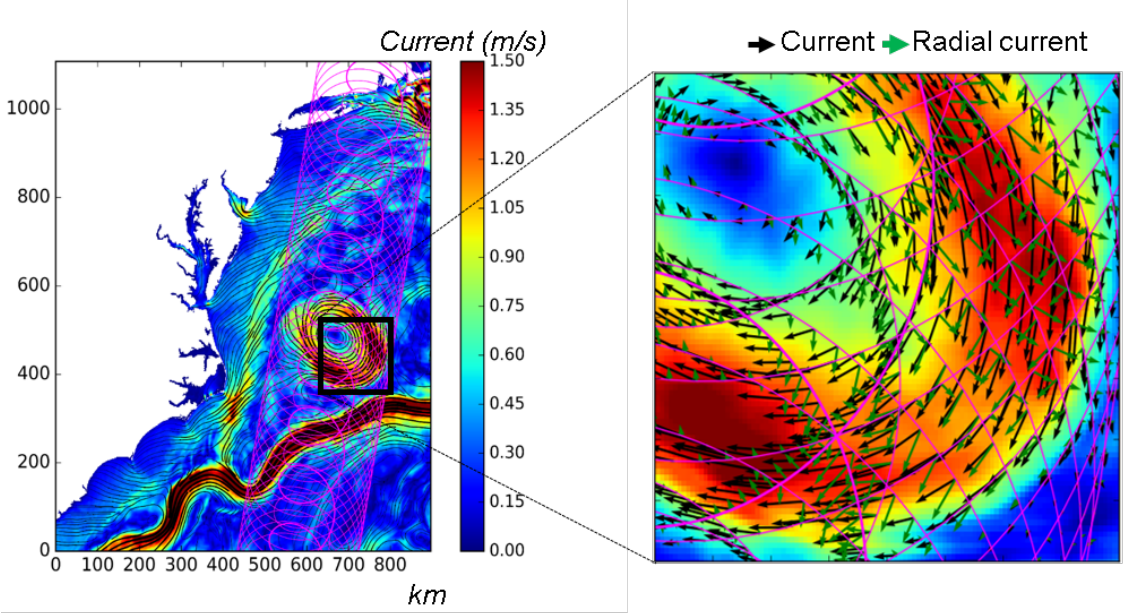

Figure 8: Detailed view of the skimulator outputs showing, with respect to the reference 2D current vectors in black, the observed radial current along the satellite look angles in green.

5 Results

5.1 Reconstruction of Geostrophic and Ageostrophic current

The figure 9 shows, on the upper panel, a snapshot of the reference zonal geostrophic component derived from the reference SSH, considered here as the reference (true) geostrophic current. The middle and bottom panels show the reconstructed fields with the basic and improved mapping respectively, at the same date. Minor differences appear with slighly finer structures in the second case. This will be quantified in 5.2

The left three panels of figure 10 is the same for ageostrophy. The reference ageostrophic field on the top is the reference total current minus the reference geostrophic current. Here, the fields at a given date are fairly different. The temporal evolution of these fields is shown for a given location on the right panel. First, we note the reference current is composed of periodic fluctuations of approximate near-inertial frequency on top of a slower signal. The spatial extension of the patterns seems somewhat larger than the mesoscale eddy band for geostrophy, probably linked to the atmospheric wind field patterns, larger than that of the Ocean. The estmimated ageostrophic field with basic mapping clearly fails on several aspects. By construction, the inertial motions are not resolved since they occur at a much higher frequency than the filtering scales of the basic mapping so the time series (blue line) does not feature oscillations. Furthermore, the low frequency component does not seem accurate. Given the moderate number of Doppler instrument revisit (as represented by the grey diamonds on the right panel) the estimation suffers from aliasing. For instance, between days 15 and 30, the observations happen to occur primarily on the top crests of the oscillations for the zonal component, leading to overestimation at low-frequency (blue curve) in this particular case. However, the estimated ageostrophic field with improved mapping is fairly different. It does resolve inertial motions, and succeeds in capturing, to some extent, their modulation and phase. The reconstruction capability is based on the degrees of freedom of the signal with respect to the number of independant observations. Since the spatial patterns of NIOs are quite large and their temporal extension exceeds a few inertial periods, a large volume in time/space can be constrained with the Doppler observations. From the reconstructed series (red line on the right panel), it is also clear that the low frequency variations of the ageostrophy current is better resolved, the aliasing issue being now mitigated.

We illustrate on Figure 11 the total current streamlines obtained with the two methods. The effect of resolving inertial motions clearly shows up on the Lagrangian trajectories, looping like actual drifter trajectories when the near inertial current amplitudes exceeds the low-frequency current.

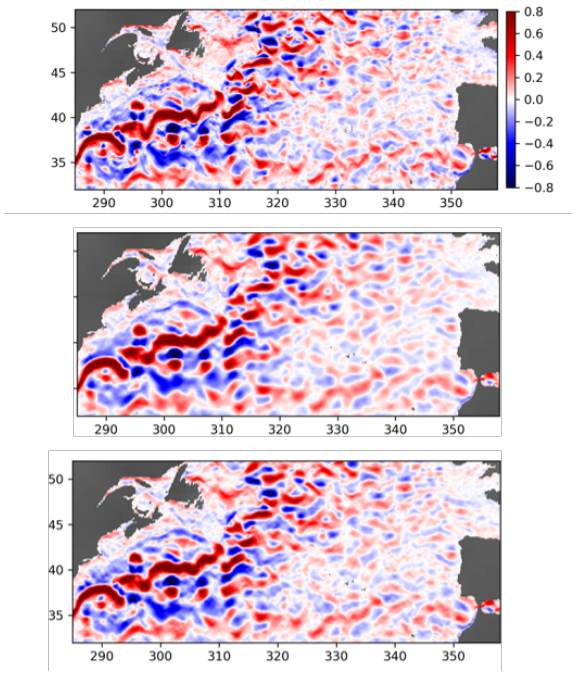

Figure 9: Reconstruction of the zonal geostrophic component (m/s) with basic mapping (middle panel) and with improved mapping (lower panel) compared to the reference (top panel).

5.2 Reconstruction skills as a function of spatial scales

The main results discussed above can be validated with a quantitative analysis of the dataset. To do so, we propose to evaluate the reconstructions as a function of spatial scales, which helps characterizing the resolving capabilities of the maps. The spectral ratio of the error (defined as the difference between the estimates and the reference) over the true signal (the reference) is computed along sections of the domain, for the cross-current variables. This computation is similar to what was proposed in (Ballarotta et al., 2019) to assess the effective resolution of Sea Surface Anomaly products. This ratio r is represented under the form of a percent score $100 * (1 - r)$ on Fig. 12 for different runs. For geostrophic reconstructions (left panel), the improvements from basic mapping (green curve) to improved mapping (red curve) are sensible at all scales, especially below 150km. If we consider 50% as a reasonable threshold, then the resolving capabilities of the altimeter reconstruction is about 110km, and 90km with SKIM combination. This is still a fair improvement for a single instrument added to an existing 5-instrument constellation. From this experiment, the Doppler observations therefore help the geostrophic component reconstruction even though Altimetry is a more direct observation of it. An additional experiment was led with improved mapping from Doppler observations only, represented in blue on the figure. The performances are not as good as with the combination, but do exceed those of altimetry only at small scales (below 250km). At large scales, the ambiguity with ageostrophy, in absence of altimetry, certainly explains the lower performances. For ageostrophic reconstructions (right panel), more sensitive differences were found as expected. Indeed, only the largest scales are partially resolved with the basic mapping. Because of aliasing issues discussed in 5.1 and the absence of NIO-like signal, the portion of resolved signal is very weak, of about 15% at 1000km wavelength. However, the reconstruction with improved mapping exceeds 50% above 500km, where most of the energy is. Note that, by construction of the sub-components for ageostrophic current, we do not aim to resolve scales below 300km. This could be explored, but doing so with this observing system would be a challenge because of high-temporal frequencies at sort spatial scales. Finally, the experiment with Doppler observations only (blue curve) brings interesting results. The drop in performances, especially at large scales, suggest the importance of an altimetry constellation the better separate the geostrophic contribution and therefore better estimate the ageostrophic component as well.

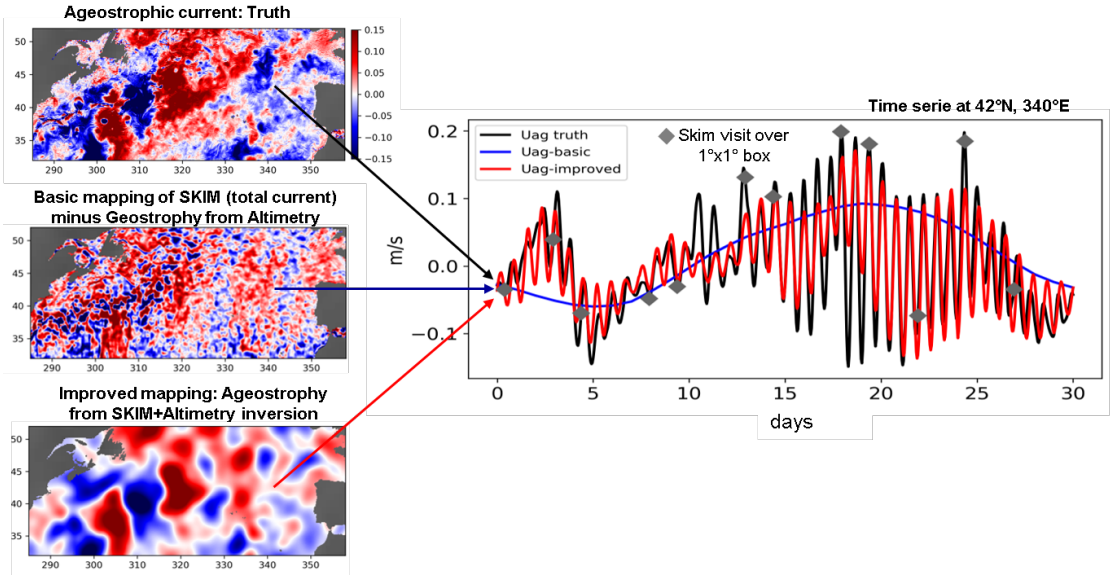

Figure 10: Reconstruction of the zonal ageostrophic component compared to the reference, in m/s. Upper left panel: snapshot of true (reference) ageostrophic zonal current. Middle left panel: reconstruction from basic mapping. Lower left panel: reconstruction from improved mapping. Right panel: time series of the reference (black), basic mapping (blue) and improved mapping (red) at 340°E, 42°N as a function of time over a month.

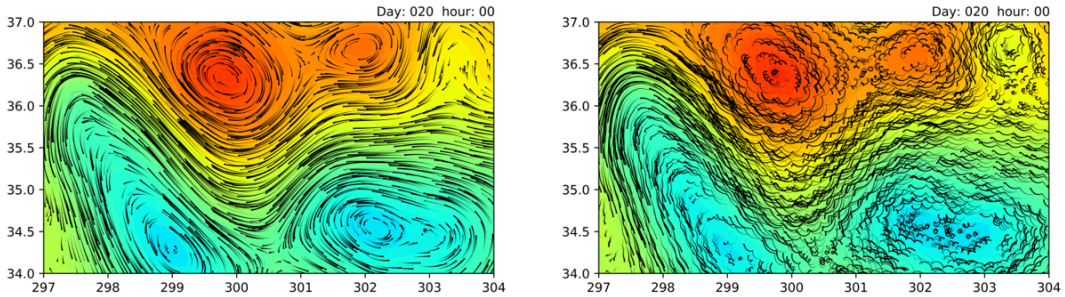

Figure 11: SSH (plain color) and streamlines (black lines) of the surface current resolved with basic (left) and improved (right) mapping.

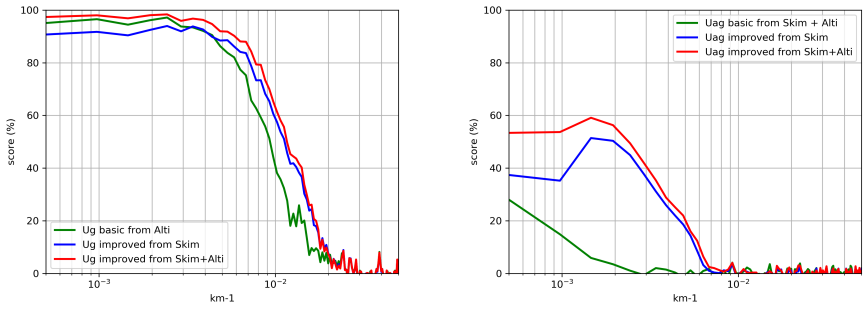

Figure 12: Quantitative assessment of the performances as a function of spatial wavelength computed, in percent, from the ratio of the reconstruction error spectrum by the true signal error spectrum. 100% means no reconstruction error. Left panel: For geostrophic current with basic mapping of Altimetry (green), with improved mapping of Skim (blue) and with improved mapping of Skim + Altimetry combined (red). Right panel: For ageostrophic current with basic mapping of Skim + Altimetry combined (green), with improved mapping of Skim (blue) and with improved mapping of Skim + Altimetry combined (red).

6 Conclusions and perspectives

This study demonstrated, in simulation, the possibility to disentangle and map various components of the Ocean surface current from partial observations of the surface dynamic topography and current. This was achieved provided a specific care to the covarience structures used in the mapping. Indeed, the time revisits of the simulated spaceborne surface current measurement exceeded inertial periods where a large part of the signal energy is. Basic mapping algorithms, acting as a low-pass filter, obviously failed in resolving those signals and were also introducing strong aliasing, as opposed to the improved mapping implemented. The performances of this later relied on the spatial and temporal coherence of high-frequency signals, long enough with respect to observation sampling. However, several additional tests (not shown) revealed that increasing the time sampling (with a wider swath design for instance) would be highly desirable even to the expense of higher instrumental noise. This should be quantified once new design options will be available. Also, from these experiments, Altimetry would remain an essential observation in addition to Doppler, in particular to disenengle the surface current components.

The reconstruction method considered in this study fully relies of the basis of sub-components chosen. This later have been constructed manually with a wavelet basis approach, accounting for coherent structures seen in the different component of the flow considered. This method has the limitation to project the observations on prescribed basis, requiring a priori knowlege of the signal characteristics ($\mathbf{G}$ matrix) and statistics ($\mathbf{Q}$ matrix). Also, the potential interactions between the components, for instance the impact of mesoscale eddies on inertial oscillations through relative vorticity fluctuations, is not yet accounted. We also acknowledge that tidal currents have not been considered is this experiment as the reference run is tide-free. However, dedicated analyses presented in (F. e. a. Ardhuin, 2019) suggest that tidal current may be well handled thanks to accurate barotropic models and favorable orbit aliasing. Baroclinic tidal current, not always phase locked (Zaron, 2019) may also be a challenge but at shorter scales a priori not interfering with inertial oscillation estimations.

As a perspective for new studies, the same approach could certainly be tested before actual spaceborne current using drifters combined with altimetry. Although the drifter distribution is sparse, their temporal sampling is very high (hourly). Since strong inertial currents were observed as spatially coherent, there might be a chance to successfully invert some near inertial current in zone of high drifter density like subtropical Gyres.

Acknowledgement

This study was funded by the Centre National d'Etudes Spatiales (CNES) as part as the Skim phase A contract for the mapping algorithm developped in section 3.3 and by the European Space Agency (ESA) as part of the Skim-SciSoc contract for the mapping algorithm implemented in section 3.2

References

Amores, Angel et al. (2018). "Up to What Extent Can We Characterize Ocean Eddies Using Present-Day Gridded Altimetric Products?" In: *Journal of Geophysical Research: Oceans* 123.10, pp. 7220–7236. DOI: 10.1029/2018JC014140. eprint: https://agupubs.onlinelibrary.wiley.com/doi/pdf/10.1029/2018JC014140. URL: https://agupubs.onlinelibrary.wiley.com/doi/abs/10.1029/2018JC014140.

Ardhuin, Fabrice et al. (2019). *Earth Explorer 9 Candidate Mission SKIM –Report for Mission Selection.*

Ardhuin, Fabrice et al. (2019a). *Estimation of Non-Geophysical Doppler and Wave Doppler, and inversion algorithm for SKIM.* DOI: 10.13140/RG.2.2.22907.98081/3.

Ardhuin, Fabrice et al. (2019b). "SKIM, a Candidate Satellite Mission Exploring Global Ocean Currents and Waves". In: *Frontiers in Marine Science* 6, p. 209. ISSN: 2296-7745. DOI: 10.3389/fmars.2019.00209. URL: https://www.frontiersin.org/article/10.3389/fmars.2019.00209.

Ballarotta, M. et al. (2019). "On the resolutions of ocean altimetry maps". In: *Ocean Science Discussions* 2019, pp. 1–27. DOI: 10.5194/os-2018-156. URL: https://www.ocean-sci-discuss.net/os-2018-156/.

D'Asaro, Eric A. (1985). "The Energy Flux from the Wind to Near-Inertial Motions in the Surface Mixed Layer". In: *Journal of Physical Oceanography* 15.8, pp. 1043–1059. DOI: 10.1175/1520-0485(1985)015<1043:TEFFTW>2.0.CO;2. eprint: https://doi.org/10.1175/1520-0485(1985)015<1043:TEFFTW>2.0.CO;2. URL: https://doi.org/10.1175/1520-0485(1985)015%3C1043:TEFFTW%3E2.0.CO;2.

Elipot, Shane, Rick Lumpkin, and Germán Prieto (2010). "Modification of inertial oscillations by the mesoscale eddy field". In: *Journal of Geophysical Research: Oceans* 115.C9. DOI: 10.1029/2009JC005679. eprint: https://agupubs.onlinelibrary.wiley.com/doi/pdf/10.1029/2009JC005679. URL: https://agupubs.onlinelibrary.wiley.com/doi/abs/10.1029/2009JC005679.

Elipot, Shane et al. (2016). "A global surface drifter data set at hourly resolution". In: *Journal of Geophysical Research: Oceans* 121.5, pp. 2937–2966. ISSN: 2169-9291. DOI: 10.1002/2016JC011716. URL: http://dx.doi.org/10.1002/2016JC011716.

Fu, Lee-Leung, Dudley B. Chelton, and Victor Zlotnicki (1988). "Satellite Altimetry: Observing Ocean Variability From Space". In: *Oceanography* 1. URL: https://doi.org/10.5670/oceanog.1988.01.

Gaultier, Lucile (2019a). *Skimulator repository.* https://github.com/oceandatalab/skimulator.

– (2019b). *Skimulator User Manual.* URL: https://github.com/oceandatalab/skimulator/blob/master/doc/source/science.rst.

Gaultier, Lucile, Clément Ubelmann, and Lee-Lueng Fu (2016). "The Challenge of Using Future SWOT Data for Oceanic Field Reconstruction". In: *Journal of Atmospheric and Oceanic Technology* 33.1, pp. 119–126. DOI: 10.1175/JTECH-D-15-0160.1. eprint: https://doi.org/10.1175/JTECH-D-15-0160.1. URL: https://doi.org/10.1175/JTECH-D-15-0160.1.

Kim, Sung Yong, P. Michael Kosro, and Alexander L. Kurapov (2014). "Evaluation of directly wind-coherent near-inertial surface currents off Oregon using a statistical parameterization and analytical and numerical models". In: *Journal of Geophysical Research: Oceans* 119.10, pp. 6631–6654. DOI: 10.1002/2014JC010115. eprint: https://agupubs.onlinelibrary.wiley.com/doi/pdf/10.1002/2014JC010115. URL: https://agupubs.onlinelibrary.wiley.com/doi/abs/10.1002/2014JC010115.

Kim, Sung Yong, Eric J. Terrill, and Bruce D. Cornuelle (2008). "Mapping surface currents from HF radar radial velocity measurements using optimal interpolation". In: *Journal of Geophysical Research: Oceans* 113.C10. DOI: 10.1029/2007JC004244. eprint: https://agupubs.onlinelibrary.wiley.com/doi/pdf/10.1029/2007JC004244. URL: https://agupubs.onlinelibrary.wiley.com/doi/abs/10.1029/2007JC004244.

Le Traon, P. Y. Le and G. Dibarboure (2002). "Velocity Mapping Capabilities of Present and Future Altimeter Missions: The Role of High-Frequency Signals". In: *Journal of Atmospheric and Oceanic Technology* 19.12, pp. 2077–2087. DOI: 10.1175/1520-0426(2002)019<2077:VMCOPA>2.0.CO;2. eprint: https://doi.org/10.1175/1520-0426(2002)019<2077:VMCOPA>2.0.CO;2. URL: https://doi.org/10.1175/1520-0426(2002)019%3C2077:VMCOPA%3E2.0.CO;2.

Pollard, R.T. and R.C. Millard (1970). "Comparison between observed and simulated wind-generated inertial oscillations". In: *Deep Sea Research and Oceanographic Abstracts* 17.4, pp. 813–821. ISSN: 0011-7471. DOI: https://doi.org/10.1016/0011-7471(70)90043-4. URL: http://www.sciencedirect.com/science/article/pii/0011747170900434.

Pujol, M.-I. et al. (2016). "DUACS DT2014: the new multi-mission altimeter data set reprocessed over 20 years". In: *Ocean Science* 12.5, pp. 1067–1090. DOI: 10.5194/os-12-1067-2016. URL: https://www.ocean-sci.net/12/1067/2016/.

Rio, M.-H., S. Mulet, and N. Picot (2014). "Beyond GOCE for the ocean circulation estimate: Synergetic use of altimetry, gravimetry, and in situ data provides new insight into geostrophic and Ekman currents". In: *Geophysical Research Letters* 41.24, pp. 8918–8925. DOI: 10.1002/2014GL061773. eprint: https://agupubs.onlinelibrary.wiley.com/doi/pdf/10.1002/2014GL061773. URL: https://agupubs.onlinelibrary.wiley.com/doi/abs/10.1002/2014GL061773.

Rodriguez, Ernesto et al. (2018). "Estimating Ocean Vector Winds and Currents Using a Ka-Band Pencil-Beam Doppler Scatterometer". In: *Remote Sensing* 10, p. 576. DOI: 10.3390/rs10040576.

Zaron, Edward (2019). "Predictability of Non-Phase-Locked Baroclinic Tides in the Caribbean Sea". In: *Ocean Science Discussions*, pp. 1–23. DOI: 10.5194/os-2019-53.